iScience

CellPress
OPEN ACCESS

Article

Bioinspired actuators with intrinsic muscle-like mechanical properties

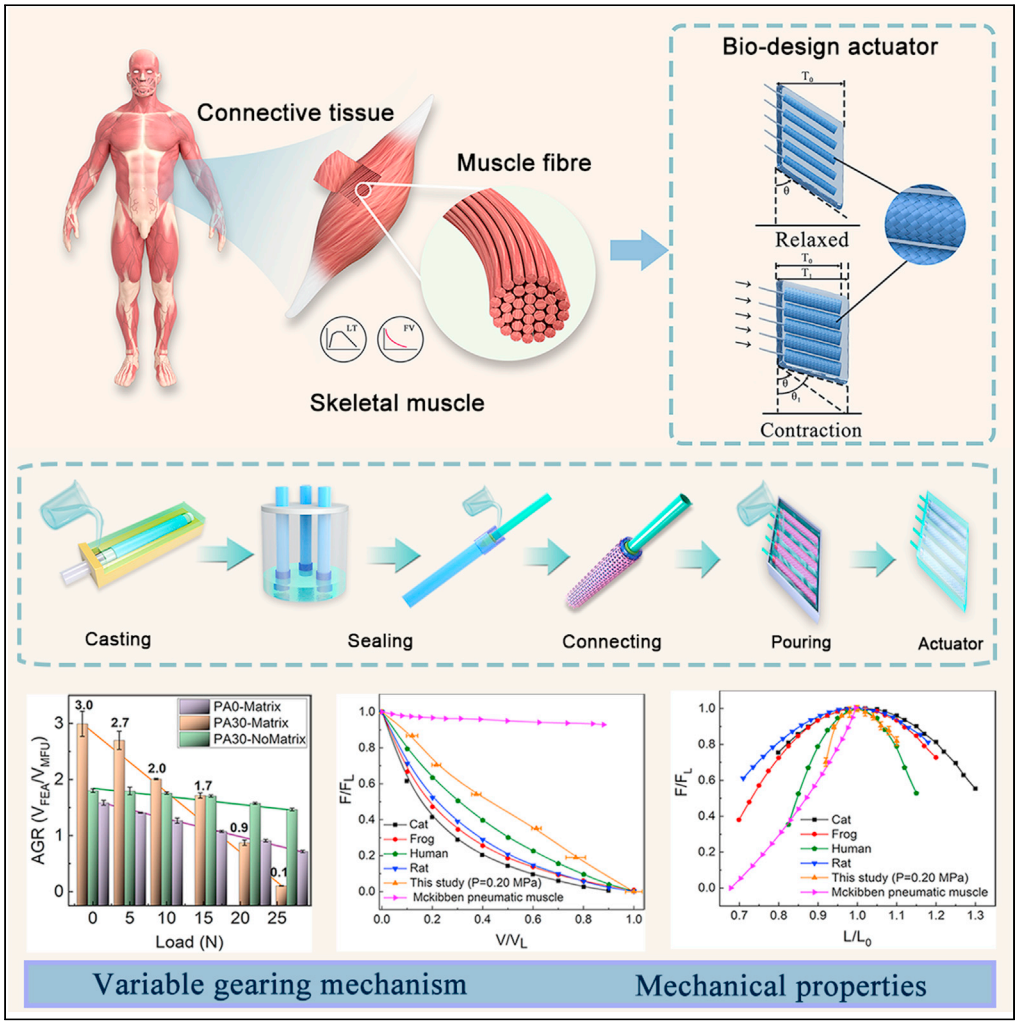

Chunbao Liu, Yingjie Wang, Zhihui Qian, ..., Guowu Wei, Luquan Ren, Lei Ren

lei.ren@manchester.ac.uk

Highlights

The actuators present intrinsic force-length and force-velocity properties

The actuators provide a variable gearing mechanism to regulate load and velocity

The actuators enable a robotic system in response to external perturbations stably

Liu et al., iScience 24, 103023
September 24, 2021
https://doi.org/10.1016/j.isci.2021.103023

iScience

CellPress
OPEN ACCESS

Article

Bioinspired actuators with intrinsic muscle-like mechanical properties

Chunbao Liu,[1,2,5] Yingjie Wang,[1,2,5] Zhihui Qian,[1] Kunyang Wang,[1] Fangzhou Zhao,[1,2] Peng Ding,[1,2] Daojie Xu,[1,2] Guowu Wei,[3] Luquan Ren,[1] and Lei Ren[1,4,6,*]

SUMMARY

Humans and animals can achieve agile and efficient movements because the muscle can operate in different modes depending on its intrinsic mechanical properties. For bioinspired robotics and prosthetics, it is highly desirable to have artificial actuators with muscle-like properties. However, it still remains a challenge to realize both intrinsic muscle-like force-velocity and force-length properties in one single actuator simultaneously. This study presents a bioinspired soft actuator, named HimiSK (highly imitating skeletal muscle), designed by spatially arranging a set of synergistically contractile units in a flexible matrix similar to skeletal musculature. We have demonstrated that the actuator presents both intrinsic force-velocity and force-length characteristics that are very close to biological muscle with inherent self-stability and robustness in response to external perturbations. These outstanding properties result from the bioinspired architecture and the adaptive morphing of the flexible matrix material, which adapts automatically to mechanically diverse tasks without reliance on sensors and controllers.

INTRODUCTION

The skeletal muscle is a powerful, flexible, and versatile actuator. Humans and animals can achieve agile, adaptable, and efficient movements because the muscle can operate in different modes depending on its intrinsic mechanical properties and morphological structures (Biewener, 2016; Neptune et al., 2009). Over the past two decades, a variety of actuator techniques have been developed to mimic skeletal muscles using materials that change dimension in response to thermal, electrical, chemical, or optical stimulations (McCracken et al., 2020; Mirvakili and Hunter, 2018; Mu et al., 2019). Most of these studies were focused on increasing the output strain, stress, or energy/power density of the actuators, whereas few studies aimed to construct actuators with muscle-like mechanical characteristics, e.g., force-velocity and force-length properties.

The contraction mechanics of the skeletal muscle has been measured and recorded in numerous muscle experiments. To interpret the results, Hill proposed a phenomenological model to describe the force-velocity and force-length dependencies of muscle force (Hill, 1938). For the force-velocity relation, he found that the muscle force decreases with increasing muscle shortening velocity in a hyperbolic form, which favors velocity output during low loads and force output against high loads. In addition, muscle force shows a parabolic force-length relationship with muscle length during an isometric contraction, where maximum isometric force is generated at resting length. The force-velocity and force-length relations are outstanding intrinsic properties of the skeletal muscle. It has been demonstrated that the force-velocity relation plays a crucial role for the stabilization of human arm movement (Brown and Loeb, 2000), human periodic hopping (Geyer et al., 2003; Haeufle et al., 2010; Wagner and Blickhan, 1999), and explosive jumping (van Soest and Bobbert, 1993). Moreover, the force-velocity and force-length relations have been shown to provide intrinsic feedback control of muscle force and work when animals encounter unexpected perturbations or require rapid adjustment during locomotion (Daley et al., 2009; Loeb et al., 1999; Rack et al., 1983). From a robotics and prosthetics point of view, it would be desirable to have an artificial actuator with similar intrinsic properties.

The McKibben pneumatic artificial muscle, developed in the 1950s for limb rehabilitation, is possibly the first attempt to construct biomechanically realistic actuators (Gaylord, 1958; Nickel et al., 1963). When being pressurized, the McKibben muscle contracts axially like the skeletal muscle due to anisotropic inflation.

[1]Key Laboratory of Bionic Engineering, Ministry of Education, Jilin University, Changchun 130022, China

[2]School of Mechanical and Aerospace Engineering, Jilin University, Changchun 130022, China

[3]School of Computing, Science and Engineering, University of Salford, Salford M5 4WT, UK

[4]Department of Mechanical, Aerospace and Civil Engineering, University of Manchester, Manchester M13 9PL, UK

[5]These authors contributed equally

[6]Lead contact

*Correspondence: lei.ren@manchester.ac.uk

https://doi.org/10.1016/j.isci.2021.103023

Unlike a biological muscle, it typically presents a concave parabolic force-length relation rather than a convex form, and also cannot be stretched beyond the resting length (Chou and Hannaford 1996; Klute and Czerniecki, 1999; Klute et al., 2002). In addition, its force-velocity relation differs from that of muscle, where force does not decrease with increasing shortening velocity (Chou and Hannaford 1996; Klute and Czerniecki, 1999; Klute et al., 2002). Yamamoto et al. fabricated a miniature McKibben actuator by silicone rubber. It is about 20mm in length and 1.0 mm in outer diameter with the output force about 234mN and strain about 10.5% by applying pneumatic pressure of 0.6Mpa (Yamamoto et al., 2012.). Kurumaya et al. fabricated a thin McKibben muscle (outer diameter 1.8 mm), which can form a multifilament actuator according to muscle shape. Multifilament actuator output force increases in proportion to the number of thin McKibben muscles. Its maximum contraction stress is about 0.30 MPa and maximum contraction ratio is 25–30%; the proposed musculoskeletal robot achieves humanlike motions by using these multifilament actuators (Kurumaya et al., 2016). They all achieved the basic research of a miniature McKibben actuator. However, the intrinsic mechanical property was not reported. To develop a more muscle-like actuator, Klute et al. constructed a mechanical system with two separate hydraulic dampers acting in parallel with a flexible pneumatic muscle. Muscle-like parabolic force-velocity characteristics were achieved, but the force-length performance remained the same as the McKibben muscle (Klute and Czerniecki, 1999; Klute et al., 2002). A new type of pneumatic artificial muscle constrained by straight fiber bundles was proposed (Saga et al., 2003; Saga and Saikawa, 2012). This simply designed actuator shows a force-velocity property similar to that of human muscle, but cannot work beyond the resting length. Schmitt et al. developed a mechanical platform that successfully reproduced the muscle-like hyperbolic force-velocity dependency (Haeufle et al., 2012; Schmitt et al., 2012). The system consists of two DC motors, two encoders, and one spring rather than a single actuator. Recently, a knitted-sleeve fluidic artificial muscle was proposed as an alternative to the McKibben muscle (Ball et al., 2016). It shows a convex parabolic force-length relation similar to skeletal muscle and can be stretched beyond the resting length. However, the force-velocity property was not reported (Ball et al., 2016). It still remains a challenge to realize both force-velocity and force-length properties of skeletal muscle in one single actuator simultaneously.

This study presents a new type of HimiSK (highly imitating skeletal muscle) actuator consisting of many synergistically actuated muscle fiber units (MFUs) arranged spatially in a flexible matrix similar to skeletal musculature. We begin by realizing a set of simple parallelogram-shaped HimiSKs using a multi-step fabrication process. By varying the arrangement of MFUs and the matrix, muscle-like force-velocity characteristics can be achieved attributing to a variable gearing mechanism provided by specially arranged MFUs embedded in a flexible matrix. Furthermore, we developed methods for numerically simulating these actuators that can provide insight into how MFU movement and matrix shape change regulate velocity output in response to different loads. To demonstrate the capabilities of this new type of HimiSK actuator, we present a specific case study of a highly anthropomorphic actuator that mimics the 3D muscle fiber arrangement and morphology of the human semimembranosus muscle. Muscle-like force-velocity and force-length relations were achieved simultaneously in this semimembranosus HimiSK actuator at different activation levels. Impact perturbation experiments on a robotic arm demonstrated that the semimembranosus HimiSK actuator can provide outstanding self-stabilizing capability compared with the McKibben actuators due to their intrinsic muscle-like mechanical properties. This class of programmable, muscle fiber executed actuators has the potential for a wide range of applications including bioinspired robotics, active prostheses and exoskeletons or rehabilitation robotics.

RESULTS

Bioinspiration and soft actuator design strategy

The skeletal muscle has been considered as a representative soft actuator because it can generate fast, strong actuation with outstanding intrinsic mechanical properties (Biewener, 2016; Josephson, 1993; Marsh, 1999). Mimicking this biological actuator with traditional robotic systems is challenging and normally involves complex mechanisms and many actuators. Even though the output of the robotic system can be modulated using advanced control methods, it is difficult to attain properties similar to biological actuator. As illustrated in Figure 1A, if we look to the skeletal muscle for inspiration, powerful actuation of soft muscular structure is achieved through the functional arrangement of many simple muscle fibers (or contractile units) arranged in an ordered spatial architecture embedded in soft connective tissues, and actuated synergistically (Josephson, 1993; Neptune et al., 2009). Furthermore, biomechanics studies show that the spatial arrangement of muscle fibers within a muscle play an important role in determining a muscle's mechanical function (Azizi et al., 2008; Brainerd and Azizi, 2005). For example, as

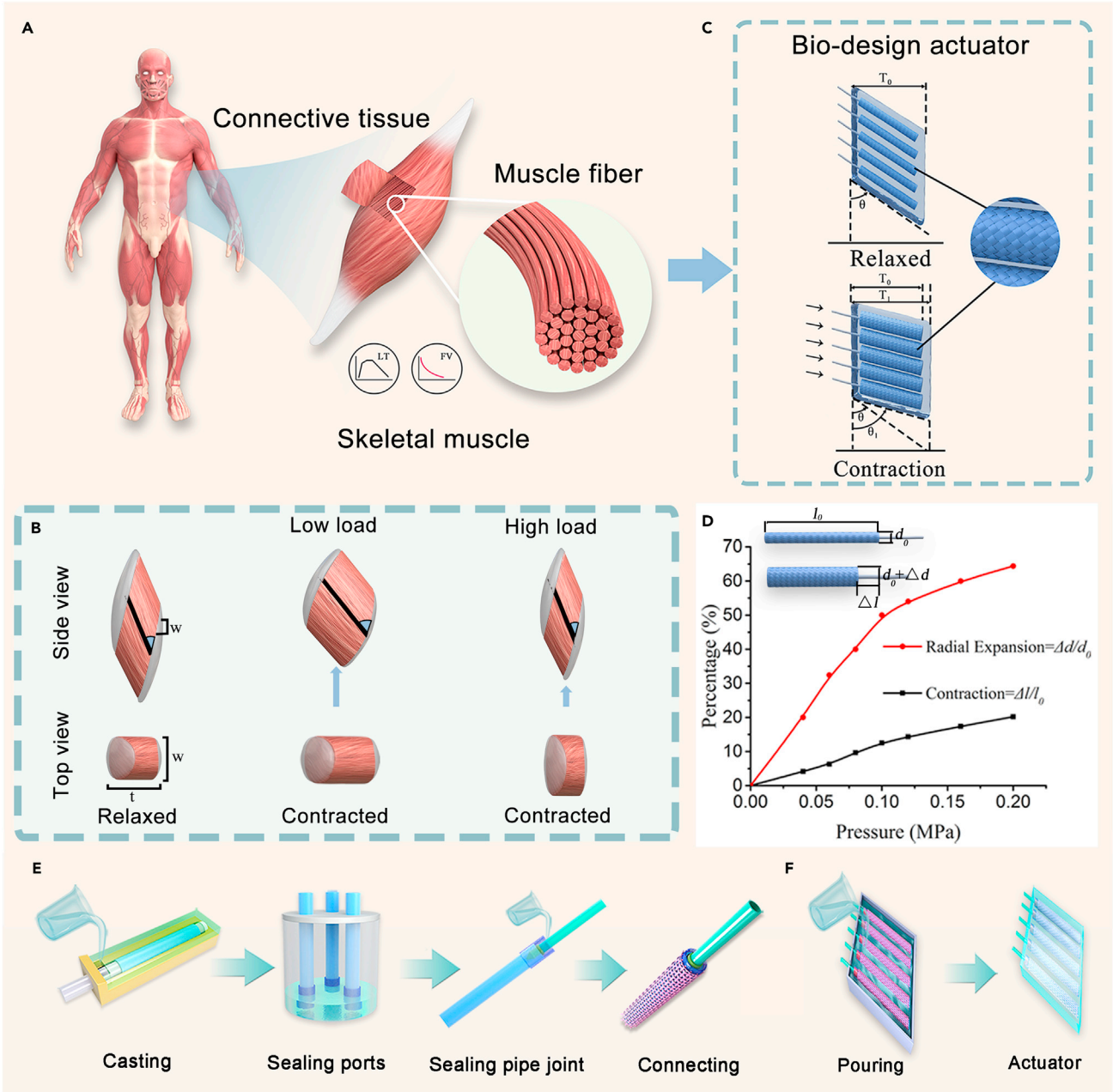

Figure 1. Bio-design, fabrication and operate principles of HimiSK actuator

(A) The structure of skeletal muscle; each muscle consists of muscle fibers and flexible connective tissue.

(B) Working principle of pennate muscle.

(C) Schematic of HimiSK actuator with pressure off and pressure on.

(D) The measured percentage changes in axial contraction and radial expansion of a single MFU under different air pressures (0.04, 0.08, 0.12, 0.16, and 0.20 MPa).

(E) Fabrication process of MFU.

(F) Fabrication process of HimiSK actuator.

depicted in Figure 1B, fibers in pennate muscles are oriented at an angle to the muscle's line of action (i.e., pennation angle). During low-load contractions, muscle contraction leads to an increase in pennation angle and muscle thickness, which results in a large amount of muscle shortening, thus favoring the velocity output of a muscle. During high-load contractions, a decrease in muscle thickness counteracts pennation angle change and results in little muscle shortening, which favors muscle force production. This variable

gearing mechanism would facilitate the reproduction of the intrinsic force-velocity relation of biological muscle (Brainerd and Azizi, 2005). Therefore, inspired by skeletal muscle architecture and biomechanics, we design a new class of HimiSK actuators, which comprise many simple contractile units (MFUs) arranged spatially in a flexible matrix similar to the muscle fiber arrangement in skeletal muscle (Figure 1C). Its working principle is that when the fluid into the cavitity, the contractile units contracted, and driving the flexible matrix produce morphology change.

Manufacturing processes

Fabrication of MFUs

We selected the McKibben pneumatic muscle to act as the MFUs for this class of HimiSK actuators. It is because McKibben muscles contract axially accompanied with radial expansion like muscle fibers, and they can be fabricated to be fully soft and easily integrated into a soft material matrix. The working principle of the fabricated MFUs is depicted in Figure 1D, their axial contraction and radial expansion are characterized and plotted as a function of input pressure. We can see that a large amount of contraction/expansion occurs at low pressures due to the low elastic modulus of the inner elastomeric tube. These soft low-threshold pressure MFUs were fabricated using a multi-step molding process similar to the method used by Ellen et al. (Roche et al., 2014). Figure 1E shows the fabrication process. For each MFU, an elastic circular tube (outer diameter: 10 mm, inner diameter: 6 mm) was fabricated by pouring prepared elastomer into a 3D printed mold (Figure 1E, casting), and with both ends sealed in a beaker forming inner elastomeric tube when they cured (Figure 1E, sealing ports). An air supply tube was secured inside the inner elastomeric tube through a pipe joint and sealed by casting elastomer (Figure 1E, sealing pipe joint). Each inner elastomeric tube was sheathed in a nylon mesh with one end fastened by a nylon cable tie and the other end sintered by heating (Figure 1E, covering), forming the final MFU (length: 110 mm). Before casting the actuators, sealing properties of each MFU is needed to be examined, which ensures the safety and reliability of actuator when applied under a high pressure. Also, the failure of the actuator is mainly caused by a rupture of MFU when the gas pressure beyond the ability of the materials to withstand the maximum pressure. Therefore, the maximum pressure of MFUs were tested before adding flexible matrix ensuring that the pressure applied to the actuator is less than the MFUs' maximum pressure.

Fabrication of parallelogram-shaped actuators

The McKibben-muscle-based MFUs are limited in that their output forces do not decrease with increasing shortening velocity. This differs considerably from the force-velocity relation of biological muscle. However, if MFUs are arranged spatially in a flexible matrix according to muscle architecture, analogous to individual contractile elements such as muscle fiber and muscle-like resultant properties may be achieved. In order to understand the behavior of a composite material system consisting of MFUs embedded in an elastomeric matrix, we fabricated a number of simple parallelogram-shaped actuators with different MFUs and matrix configurations. The fabrication process is shown in Figure 1F. Parallelogram molds include 4-mm diameter side holes to support air supply tubes. Before casting the actuators, the MFU array and supply lines were placed in the mold based on predefined pennation angle arrangement, and prepared elastomer were poured into the mold case (Figure 1F, Pouring). The finished flexible matrix was finally solidified at room temperature; the volume of PA30-Matrix actuator was 0.0001785 m^3 (Figure 1F, actuator). More fabrication details are described in the STAR Methods. Finally, three parallelogram-shaped HimiSK actuators each consisting of five MFUs were fabricated. These include 0° and 30° pennation angle arrangements with flexible matrix (denoted as PA0-Matrix and PA30-Matrix respectively), and also 30° pennation angle configuration without matrix (PA30-NoMatrix), as shown in Figure 2A. This allows us to investigate the effect of MFU pennation angle and flexible matrix on the actuator's performance without considering the complex MFU architecture and matrix morphology in three-dimensional. When air pressure is applied, the MFUs contraction, and driving the flexible matrix to produce morphology change, thus realizing linear contraction and force output (Figure 2B). In addition, the flexible matrix, which wrapped around the MFUs directly, will prevent the MFUs from being stretched. In addition, the flexible matrix made of silicone rubber has good flexibility, high elasticity, and strong tensile strength properties. It can bear repeatedly stretching when contracting under high loads.

Effect of MFU arrangement and flexible matrix

To characterize the actuators' force-velocity properties, the three actuators were tested using a customized test-rig (Figure S1). To start the dynamic contraction of the soft actuator, a valve was opened which allowed

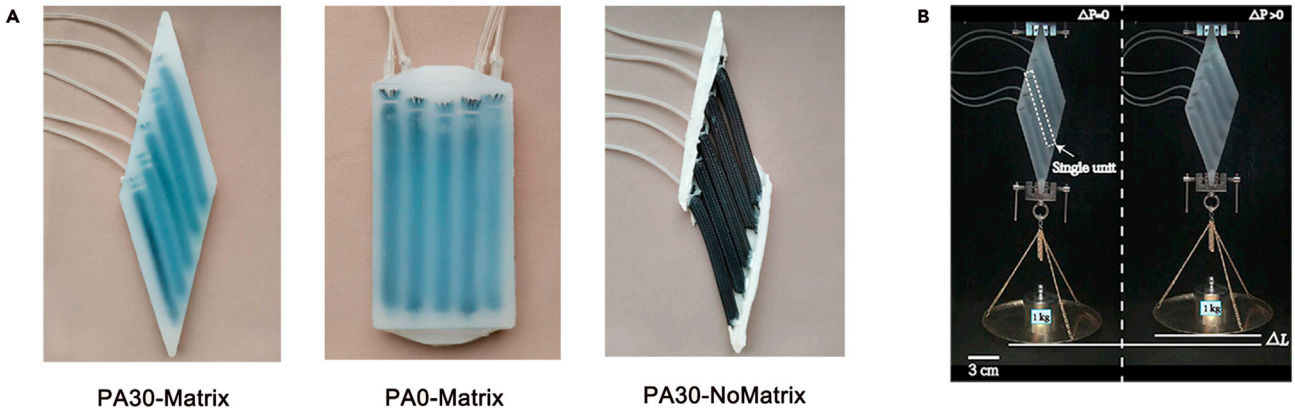

Figure 2. The parallelogram-shaped HimiSK actuators

(A) Three finished HimiSK actuators: PA30-Matrix, PA0-Matrix, and PA30-NoMatrix

(B) PA30-Matrix actuator lifting 1 kg loads on application of air pressure at 0.2 MPa.

inflation of all MFUs simultaneously. The actuator contracted and lifted the load until it shortened maximally, at which point the air was released from all the MFUs. The actuators were tested at five air pressures (0.04, 0.08, 0.12, 0.16, 0.20 MPa), and the maximum load F_0 that the actuator can lift was determined at each pressure. The actuator acted against 6 different loads ranging from 0 to 100% F_0 with a 20% F_0 increment (see Video S1). The test was repeated six times at each load for each pressure. Four variables were obtained for each trial including MFU shortening velocity, actuator shortening velocity, pennation angle, and actuator thickness. More details on the experimental testing and data analysis (Figure S2) are described in the STAR Methods.

For all the three actuators (PA30-Matrix (Figure 3A), PA0-Matrix (Figure 3B), and PA30-NoMatrix (Figure 3C)), during nearly all contractions, the shortening velocity of MFU does not particularly change with increased load (Figures 3D–3F), which is consistent with previous experimental results on McKibben pneumatic muscle (Chou and Hannaford 1996; Klute and Czerniecki, 1999). However, from Figures 3G–3I, we can see that the shortening velocity of the actuator shows an apparently different trend. Their shortening velocities decrease noticeably with an increasing load similar to skeletal muscle. The shortening velocity of the actuator exceeds the shortening velocity of the MFUs. This indicates an inherent gearing mechanism for output velocity amplification, which can be quantified as the ratio of whole actuator velocity to MFU contraction velocity, similar to a relation describing a muscle's architectural gear ratio (AGR) (Brainerd and Azizi, 2005). The calculated AGRs (Figures 3J–3L) show a significantly decreasing trend with increasing load across contractions at different levels of pressures. This variable gearing mechanism is similar to the phenomenon that has been observed in pennate muscles (Azizi et al., 2008). This suggests that like skeletal muscles the parallelogram-shaped HimiSK actuators with a variable gearing mechanism that shifting from a high AGR during rapid contractions to a low AGR during forceful contractions. In addition, the measured pennation angle and actuator thickness (Figures S3) show decreasing load-dependent patterns during all contractions for all the three actuators (detailed in STAR Methods). This highly coincides with the load-dependent pattern of AGRs suggesting that the variable gearing mechanism results from the MFU pinnate arrangement and the shape change of the flexible matrix similar to the skeletal muscle (Figure 1B).

To better understand the effect of MFU arrangement and the flexible matrix, we compare the load dependencies of pennation angle, actuator thickness, AGR, and force-velocity relations of the three actuators at the air pressure of 0.20 MPa. Figure 3M shows that the pennation angle decreases more rapidly with an increasing load when MFUs are not embedded in a flexible matrix (PA30-Nomatrix). This is probably because a flexible matrix can constrain the rotation of MFUs due to the interface pressures. Figure 3N shows that all the three actuators demonstrate similar decreasing slopes with increased load for the actuator thickness. The AGR of PA30-Matrix presents the largest working range among all three actuators (Figure 3O). It operates at the highest gear ratio of 2.99 at zero load among all actuators indicating that the actuator velocity is amplified 199% relative to the MFU velocity. Conversely, when acting against the

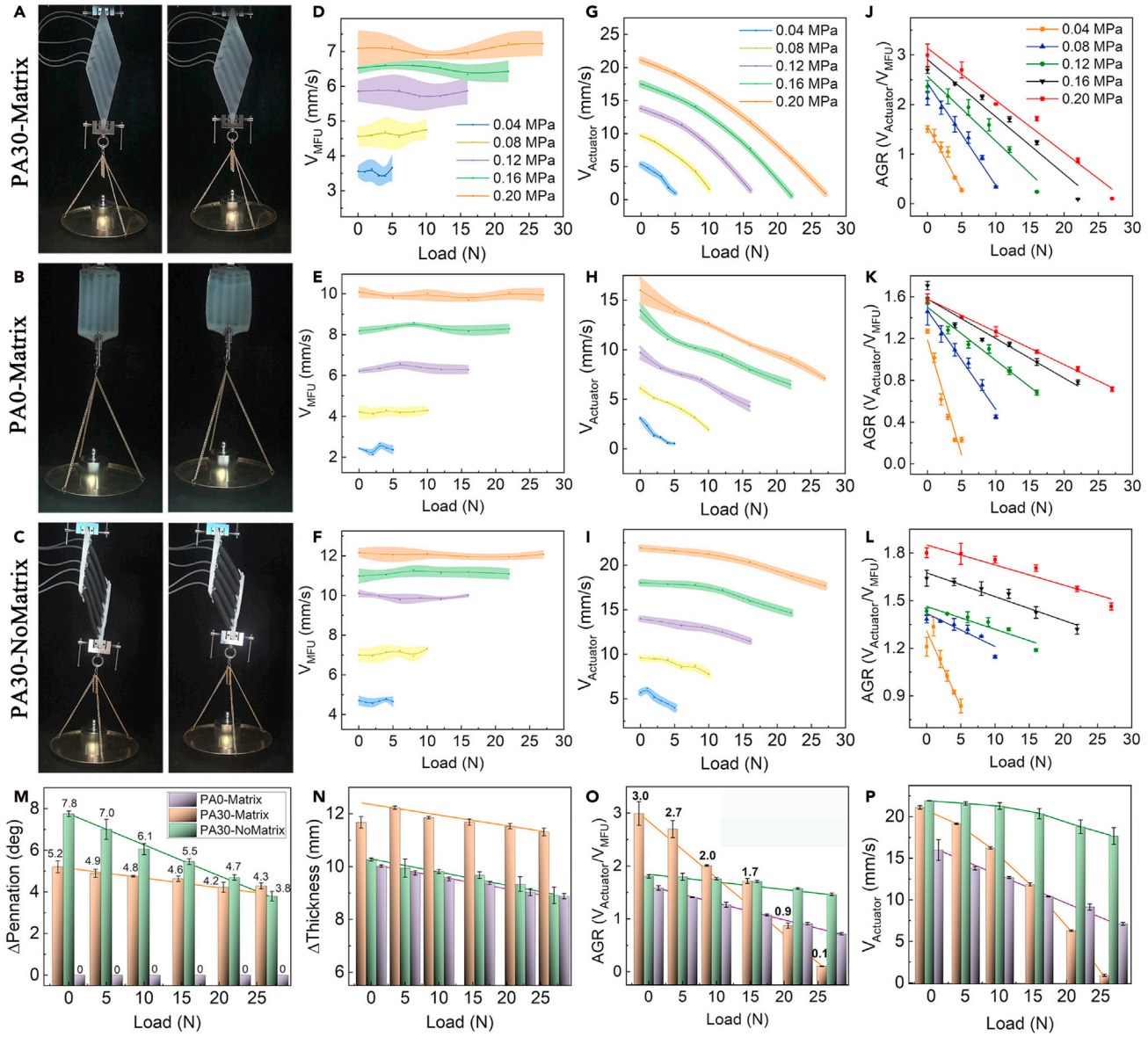

Figure 3. Effect of MFU Arrangement and Flexible Matrix

(A) Contraction of PA30-Matrix actuators.

(B) Contraction of PA0-Matrix actuators.

(C) Contraction of PA30-NoMatrix actuators.

(D–F) Changes in MFUs contraction velocities.

(G–I) Changes in actuators contraction velocities.

(J–L) Load-dependent AGRs for each actuator at different air pressures.

(M) Changes in pennation angles at 0.2 MPa.

(N) Changes in thicknesses at 0.2 MPa.

(O) Changes in AGRs at 0.2 MPa.

(P) Force-velocities of three actuators at 0.2 MPa. All the error bars denote S.D.

maximum load, it operates at the lowest gear ratio of 0.10 among all actuators corresponding to a 90% reduction in velocity. PA0-Matrix shows a much smaller gearing range, whereas PA30-NoMatrix presents the smallest working range. This suggests that both MFU architecture and flexible matrix have substantial effects on the variable gearing mechanism, and it appears that the contribution of the actuators configured in a pennate is slightly larger than that of the flexible matrix. This is well reflected in the force-velocity

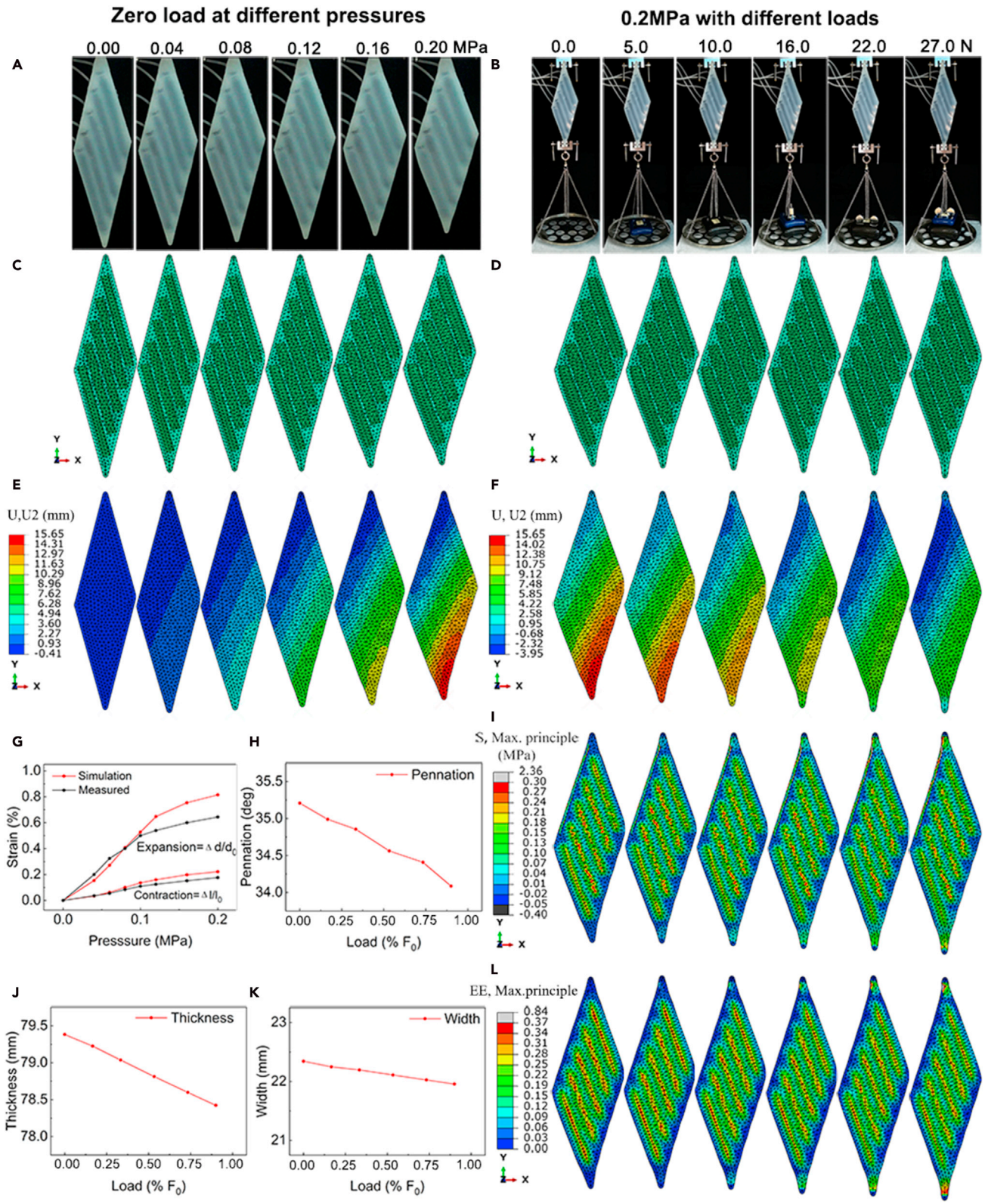
Zero load at different pressures
0.00
0.04
0.08
0.12
0.16
0.20 MPa
A
0.2MPa with different loads
0.0
5.0
10.0
16.0
22.0
27.0 N
B
C
D
E
U,U2 (mm)
15.65
14.31
12.97
11.63
10.29
8.96
7.62
6.28
4.94
3.60
2.27
0.93
-0.41
F
U, U2 (mm)
15.65
14.02
12.38
10.75
9.12
7.48
5.85
4.22
2.58
0.95
-0.68
-2.32
-3.95
G
Simulation
Measured
Strain (%)
Expansion= Δ d/d0
Contraction= Δ l/l0
Presssure (MPa)
H
Pennation
Pennation (deg)
Load (% F0)
I
S, Max. principle
(MPa)
2.36
0.30
0.27
0.24
0.21
0.18
0.15
0.13
0.10
0.07
0.04
0.01
-0.02
-0.05
-0.40
J
Thickness
Thickness (mm)
Load (% F0)
K
Width
Width (mm)
Load (% F0)
L
EE, Max.principle
0.84
0.37
0.34
0.31
0.28
0.25
0.22
0.19
0.15
0.12
0.09
0.06
0.03
0.00

Figure 4. Numerical Modeling of Deformations of the PA30-Matrix actuator

(A) The recorded deformations of the unloaded PA30-Matrix actuator at different pressures (0, 0.04, 0.08, 0.12, 0.16 and 0.20 MPa).
(B) The recorded deformations of the PA30-Matrix actuator when acting against increased load (0, 5, 10, 16, 22 and 27 N) at an air pressure of 0.2 MPa.
(C) Simulated mesh deformation at different pressures.
(D) Simulated mesh deformation at different loads.
(E) Vertical displacement distribution at different pressures.
(F) Vertical displacement distribution under different loads at 0.2 MPa.
(G) Comparison of the simulated (red) and measured (black) radial expansion and axial contraction of a single MFU.
(H) Simulated changes in the pennation angle.
(I) Maximum principal stress.
(J) Simulated changes in thickness.
(K) Simulated changes in width.
(L) Maximum principal strain.

relations of the three actuators (Figure 3P). The PA30-Matrix presents a most muscle-like load-dependent velocity property capable of generating great force during forceful contractions (low velocity) and large velocity during rapid contractions compared with PA0-Matrix, PA30-NoMatrix actuators (Figure 3P).

These results demonstrate that when MFUs embedded in a flexible matrix with a pennate arrangement, the parallelogram HimiSK actuator can present a muscle-like force-velocity property. This results from a variable gearing mechanism, which is automatic owing to the intrinsic mechanical behavior that emerges from the actuator material and architecture. Such an intrinsic characteristic enables the actuator to respond to changes in mechanical loading conditions rapidly without the need of sensory information or feedback control.

Numerical Modeling of Deformations

Having tested the three actuators, we developed a numerical model of the PA30-Matrix actuator to simulate our soft actuated materials. The simulations were conducted using the finite element analysis software ABAQUS and provide a means to predict the performance of the soft active materials at different pressures and under different loads (Figures 4A and 4B). To simulate the response of the actuator to an increase in air pressure, we modeled the MFUs as closed circular tubes driven by fluid cavity, which is capable of simulating pressured gas or liquid behavior. Double symmetrical layer rebars were used to model the woven meshes wrapping around the MFUs and the flexible matrix was modeled as an elastic material (described further in STAR Methods). The top end of the actuator was fixed while the load was applied at the bottom end to replicate the loading and boundary conditions in the experiments. The simulation output was pennation angle, actuator thickness and width, displacement, and also strain and stress distributions of the flexible materials.

Analysis at zero loads under different pressures

First, we compare the numerical and experimental results of the longitudinal shortening and radial expansion strains for a single MFU component at different pressures (Figure 4G). Good agreements can be seen for the strains at both directions.

Then, the PA30-Matrix actuator at different pressures without load was simulated. As expected, the soft actuator was actuated by five MFUs synergistically (Figure S4), we also observe increasing actuator contraction, pennation angle and actuator thickness associated with increased pressure (Figures 4C and 4E). This is consistent with our observation of the actuator shape changes in the experiments (Figure 4A).

Analysis at 0.2MPa with different loads

Afterward, when the pressure is kept at 0.2 MPa with gradually increased load, the model predicted the load-dependent changes in the deformation (Figure 4D), vertical displacement (Figure 4F), maximum principal strain (Figure 4I) and maximum principal stress distributions (Figure 4L) of the active material (see Video S2). The model also predicted the changes in the mid/min principal strain, mid/min principal stress distributions (Figure S5). At low loads, large displacements are generated in the entire actuator with high strains mainly in the MFUs due to the pressurized air, which tends to enlarge contraction velocity and hence favors speed output. At high loads, the actuator displacements are greatly reduced with high tensile strains in the MFUs and also the flexible matrix with a tendency to lessen contraction speed, which facilitates force output. The predicted pennation angle and actuator thickness (Figures 4H and 4J) decrease with increased

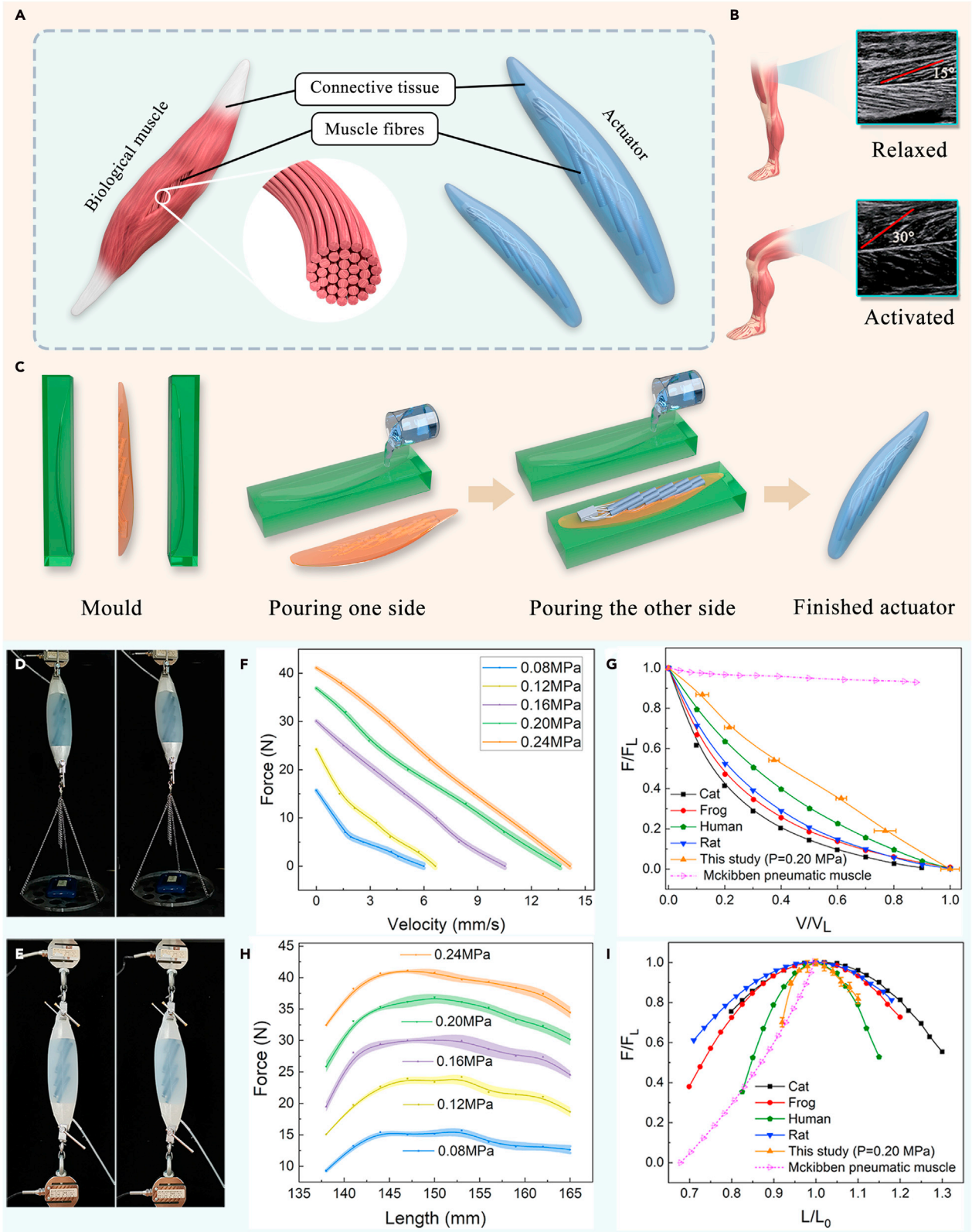
A
Biological muscle
Connective tissue
Muscle fibres
Actuator
B
15°
Relaxed
30°
Activated
C
Mould
Pouring one side
Pouring the other side
Finished actuator
D
E
F
0.08MPa
0.12MPa
0.16MPa
0.20MPa
0.24MPa
Force (N)
Velocity (mm/s)
G
F/FL
Cat
Frog
Human
Rat
This study (P=0.20 MPa)
Mckibben pneumatic muscle
V/VL
H
0.24MPa
0.20MPa
0.16MPa
0.12MPa
0.08MPa
Force (N)
Length (mm)
I
F/FL
Cat
Frog
Human
Rat
This study (P=0.20 MPa)
Mckibben pneumatic muscle
L/L0

Figure 5. Highly anthropomorphic muscle-like actuators

(A) The anatomical morphology of the human semimembranosus muscle.

(B) Two *in vivo* ultrasound images of pennation angle of the left semimembranosus muscle from 15° at relaxed condition to 30° at fully activated condition.

(C) Fabrication process of the semimembranosus HimiSK actuator.

(D) Isotonic contraction test.

(E) Isometric contraction test.

(F) Force-velocity properties of the actuator under five different activation pressures.

(G) The normalized force-velocity relationship of the actuator at 0.2 MPa compared to those of cat, frog, human, rat and also McKibben pneumatic muscle.

(H) Force-length properties of the actuator under five different activation pressures.

(I) The normalized force-length property of the actuator at 0.2 MPa compared to those of cat, frog, human, rat and also McKibben pneumatic muscle. All the error bars denote S.D.

load, whereas no obvious change is found in actuator width (Figure 4K). Based on the PA30-Matrix actuator numerical simulation, the work density and efficiency (η) at 0.2MPa was also calculated and detailed in STAR Methods.

Our simulation results suggest that the variable gearing mechanism presented in the parallelogram-shaped HimiSK actuator is mediated by the obliquely oriented MFUs and the flexible matrix material that control the shape changes that alter gearing. At low-load contraction, the increased MFU rotations and small tensile strains in matrix material tends to increase actuator displacement and hence contraction velocity. At forceful contraction, the decreased MFU rotations and large tensile strain in the flexible matrix has a tendency to reduce the actuator contraction velocity, thus favoring force output. This indicates that the pennated arrangement of the MFUs and the softness of the matrix material provide the critical regulation of actuator shape change, and the automatic variable gearing mechanism is achieved by the intrinsic morphological and material properties of the soft actuator without reliance on any active controls.

Highly anthropomorphic muscle-like actuators

Upon establishing the fabrication approach, accomplishing the experimental characterization, and developing a numerical simulation method, we then took inspiration from the human semimembranosus muscle to create an anthropomorphic HimiSK actuator, termed semimembranosus HimiSK actuator. The human semimembranosus is a flat, long muscle with a typical pennated musculature (Figure 5A). The muscle fibers are arranged obliquely in the connective tissue considering the MFU architecture and matrix morphology is three-dimensional. We measured the semimembranosus muscle fiber architecture of a healthy male subject using an ultrasound scanner (measuring process is detailed in STAR Methods). The muscle fiber arrangement with the subject lying supine (Figure 5B) and the pennation angle change during knee flexion were recorded (see Video S3). Informed by this ultrasound measurement, an anthropomorphic HimiSK actuator was fabricated with identical dimensions and geometry to the semimembranosus muscle. Figure 5C describes the multi-step molding process using a 3D printed three-part mold that included alignment features for accurately embedding multiple MFUs in a flexible matrix. The first step secured ten MFUs and their air supply tubes in the left half of the flexible matrix in a two-layer three-dimensional architecture. The second step finished the whole actuator by pouring elastomer into the right half mold, which resulted in a semimembranosus HimiSK actuator with a length of 225.28 mm and a maximum thickness of 60 mm. The fabrication process is described further in the STAR Methods.

To characterize the force-velocity and force-length properties of the semimembranosus HimiSK actuator, mechanical tests were conducted during both isotonic (Figure 5D) and isometric (Figure 5E) contractions at five different air pressures (0.08, 0.12, 0.16, 0.20, 0.24 MPa) using two customized test rigs (Figures S1 and S7), respectively. The experimental testing and data acquisition are detailed in the STAR Methods. The actuator force presents a consistent decreasing pattern with increased velocity across different levels of activation pressures (Figure 5F). Like the skeletal muscle, the output force increases with increasing activation level, and the maximum force is generated at very low speed during forceful contractions, whereas zero force is produced at maximum contraction velocity. Figure 5G compares the normalized force-velocity relation of the HimiSK actuator at 0.20 MPa with those of rat (Bahler, 1968), cat (Wilkie, 1956), frog (Mccrorey et al., 1966) and human muscles (Ralston et al., 1949) and also that of McKibben pneumatic muscle (Chou and Hannaford 1996; Klute and Czerniecki, 1999). We can see that the HimiSK actuator presents a force-velocity property that is much more comparable to human muscle than McKibben pneumatic muscle. This indicates that our bioinspired semimembranosus HimiSK design successfully transforms the force-velocity property of the McKibben-muscle-based MFUs into a muscle-like characteristic.

During isometric contractions, the force-length relation of the semimembranosus HimiSK actuator shows a consistent concave downward parabolic form across different levels of activation pressures (Figure 5H). Similar to the skeletal muscle, the output force is larger at higher activation levels. Figure 5I shows the normalized force-length relations of the semimembranosus HimiSK actuator (at 0.20 MPa), rat (Bahler, 1968), cat (Wilkie, 1956), frog (Mccrorey et al., 1966) and human muscles (Ralston et al., 1949) and also the McKibben pneumatic muscle (Chou and Hannaford 1996; Klute and Czerniecki, 1999). We can see that the semimembranosus HimiSK actuator presents a parabolic force-length curve that is very close to human muscle. It can also be stretched beyond the resting length like the biological muscle in contrast to the McKibben pneumatic muscle. In summary, these results demonstrate that a single actuator with both intrinsic muscle-like force-velocity and force-length properties simultaneously can be achieved by using the bioinspired HimiSK method proposed in this study.

Performance on High-Speed Stabling

To assess the dynamic performance of the semimembranosus HimiSK actuator, we performed impact perturbation experiments on a robotic arm with a revolute joint regulated by a pair of antagonistic HimiSK actuators (Figure 6). The robotic arm consists of a fixed vertical upper arm and a moving forearm. The revolute elbow joint is constrained by a pair of identical HimiSK actuators, which are activated at the same air pressure (0.05 or 0.20 MPa). This makes the elbow joint balanced at an angle of 90° holding the forearm in a horizontal level position. A gas-powered cylinder was used to apply downward or upward impact perturbation to the end tip of the forearm. The gas cylinder was powered at a pressure of 0.5 MPa for 25 ms regulated by a control system to generate consistent and repeatable impact force (described in STAR Methods and Figure S8). A marker was placed near the end tip of the forearm, and a high-speed camera was used to capture the robotic arm motions at 1000 Hz. The recorded video data was digitized to obtain the marker coordinates (X, Y) and the forearm angle θ. To compare with McKibben pneumatic muscle, we repeated the impact perturbation experiments on the robotic arm when the elbow joint was regulated by an antagonistic pair of identical McKibben muscles (Figure 6). The McKibben muscles generated the same amount of forces as the HimiSK actuators upon being pressurized.

Figures 6A–6D show the end tip marker trajectories (plotted every 1ms) and the time histories of the forearm angle of the robotic arm with McKibben muscles (activated at 0.05 and 0.20 MPa) when downward impact perturbation was applied. Compared with the corresponding results with HimiSK actuators (Figures 6E–6H), we can see that the robotic arm experienced periodic oscillations with much larger amplitudes, and spent much longer time to revert back to its original stable position when McKibben muscles were employed. The same tendency is also found in the recorded forearm motions during the upward impact perturbation experiments (Figures 6I–6P). For both downward and upward impact perturbations and for both muscle activation pressures, the results consistently indicate that the HimiSK actuator can significantly reduce the forearm oscillation amplitude and also the time used to return back to the original stable state in contrast to the McKibben muscle (see Video S4). For example, the first peak amplitude of the forearm angle is reduced by 38.5%, and the return time back to the original stable position is decreased by 45.8% when the McKibben muscles were replaced by the HimiSK actuators for the downward impact perturbations when the muscle activation pressure was 0.05MPa (Figures 6B vs. 6F).

These results suggest that like skeletal muscles, the HimiSK actuator is capable of providing robust response to external perturbations. Such an intrinsic characteristic enables the actuator to respond to changes in mechanical loading conditions rapidly without the need of sensory information or feedback control. This self-stabilizing capability greatly expands the range of mechanical performance of the HimiSK actuator compared with the McKibben muscle, and could reduce the dependency on feedback control in response to load changes under some conditions. This results from the muscle-like intrinsic force-velocity and force-length properties of the HimiSK actuator that emerges from the actuator material and architecture, rather than being generated by any control mechanism.

DISCUSSION

This study introduced the design, fabrication, and performance of a new type of soft HimiSK actuator, which involves embedding a set of simple contractile units (MFUs) in a flexible matrix based on a specific spatial arrangement by mimicking muscle architecture. We have demonstrated that the semimembranosus HimiSK artificial muscle presents both intrinsic force-velocity and force-length characteristics of biological muscles with inherent self-stability and robustness in response to external perturbations. The actuator also

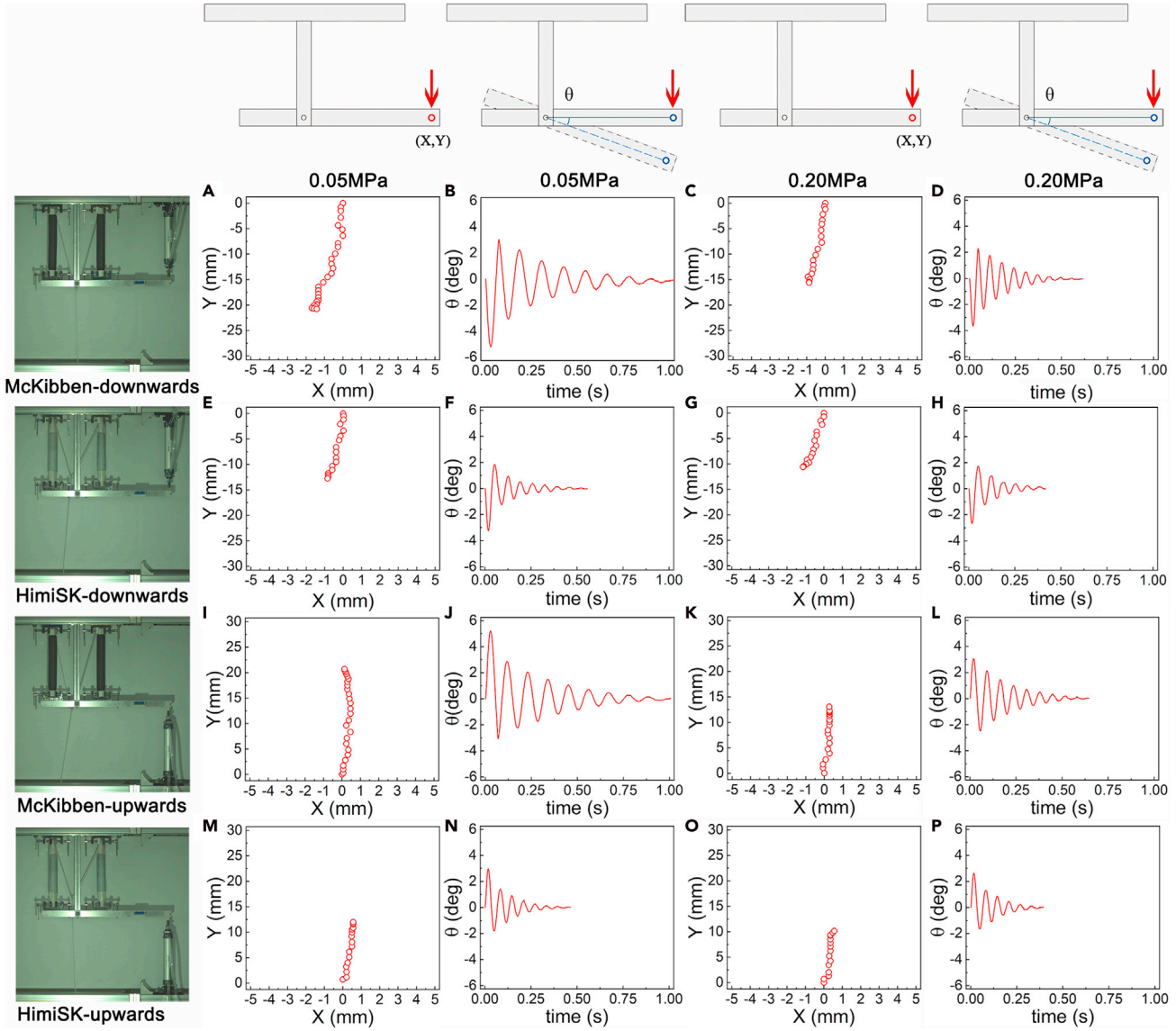

Figure 6. Performance on high-speed stabling

(A, E, I, and, M)(A), (E), (I), (M) The recorded trajectories of the end tip marker at an air pressure of 0.05 MPa.

(B, F, J, and, N)(B), (F), (J),(N) The time histories of the forearm angle of the robotic arm when the actuators were activated at an air pressure of 0.05 MPa.

(C, G, K, and, O)(C), (G), (K),(O) The end tip marker trajectories at an air pressure of 0.20 MPa.

(D, H, L, and, P)(D), (H), (L),(P) The time histories of the forearm angle when the actuators were pumped at an air pressure of 0.20 MPa.

possesses an intrinsic variable gearing mechanism providing an automatic transmission system, in which the trade-off between force and velocity is self-regulated to modulate muscle performance during mechanically diverse functions. Usually variable transmissions are cumbersome and complex with gears, clutches, and actuators. However, the HimiSK actuator shows an elegant and simple variable transmission that is directly integrated in pennate MFUs and exploits the adaptive morphing of the flexible matrix.

As revealed by the experimental testing and numerical analysis, these outstanding properties of the HimiSK actuator mainly result from the bioinspired MFUs pinnate arrangement, and also the load-dependent shape change of the flexible material, which adapt automatically to a specific task without reliance on sensors and controllers. This mechanical intelligence benefitting from bioinspired soft materials could facilitate the morphological computation of biorobotic systems (Mintchev and Floreano, 2016;

Pfeifer et al., 2007). Further tuning of the flexible materials may include using an inhomogeneous and/or anisotropic matrix to tune the material compliance, or using other types of actuators for MFUs, such as the miniature MFUs (Yamamoto et al., 2012; Kurumaya, 2016). Indeed, the presented bioinspired design concept is a template, which is not limited to using McKibben pneumatic muscles as contractile elements but also allows the use of smaller, more efficient, more powerful new actuators, for example, dielectric elastomers (Duduta et al., 2016) or carbon nanotube muscles (Chun et al., 2014; Lima et al., 2012).

Muscle-like soft actuators with biomechanically realistic mechanical properties may find many potential applications, e.g., bioinspired robotics, active prostheses, and exoskeletons or rehabilitation robotics (Cianchetti et al., 2018; Ijspeert, 2014; Yang et al., 2018). Additionally, this material platform could function as a test bed for understanding the fundamental mechanism of skeletal muscles by investigating the interplay of musculature and its mechanical properties. More generally, this study suggests that muscle-like soft actuator design may benefit from a consideration of the resultant performance of assembling a group of actuators inspired by the architecture of biological muscles, rather than only the mechanical behavior of single force-generating units.

Limitations of the study

The HimiSK actuator bioinspired from architecture and the adaptive morphing of the flexible matrix material presents both intrinsic force-velocity and force-length characteristics that are very close to biological muscle with inherent self-stability and robustness in response to external perturbations. However, the addition of a flexible matrix blocks the contraction of MFUs. Therefore, the material property and volume of flexible matrix are the main influencing factors. It is a solution to this problem by placing a large amount of muscle fibers in a limited structure and using a softer flexible matrix material. First, increasing the number of MFUs in the flexible matrix can reduce the volume of the flexible matrix. This will improve the capability of force generation and also reduce the shortening resistance of MFUs, thus improving the strain of the soft actuator. In addition, the capability of actuators for deformation can be exploited by using softer flexible matrix materials and developing bionic muscle tendon as well. This will decrease the shortening resistance of MFUs directly and eliminate the large deformations where loads are applied, thus improving the strain of the soft actuator.

STAR★METHODS

Detailed methods are provided in the online version of this paper and include the following:

- KEY RESOURCES TABLE
- RESOURCE AVAILABILITY
  - Lead contact
  - Materials availability
  - Data and code availability
- METHODS DETAILS
  - Fabrication of actuators
  - Force-velocity test and data collection
  - Thickness, pennation angle and AGR test
  - FEM simulation of PA30-Matrix actuator
  - Analysis of work density and efficiency
  - Ultrasound muscle measurement
  - Force-length property test
  - Geometric details for robotic arm
  - Impact perturbation experiments

SUPPLEMENTAL INFORMATION

Supplemental information can be found online at https://doi.org/10.1016/j.isci.2021.103023.

ACKNOWLEDGMENTS

This work is partly supported by the projects of National Natural Science Foundation of China (Grant No. 91948302 and No. 91848204), the project of National Key R&D Program of China (No. 2018YFC2001300)

and the projects of UK Engineering Physical Science Research Council (EP/K019759/1 and EP/I033602/1), the projects of National Natural Science Foundation of China (No. 52075216 and No. 51675222).

AUTHOR CONTRIBUTIONS

Conceptualization, L. Ren, C. Liu and L.Q. Ren; Validation, Y. Wang and P. Ding; Formal Analysis, Z. Qian; Investigation, Y. Wang, P. Ding, F. Zhao and D. Xu; Writing – Original Draft, L. Ren, K. Wang, Y. Wang and G. Wei. Writing – Review & Editing, all authors; Supervision, L. Ren; Funding Acquisition, L. Ren, C. Liu and Z. Qian.

DECLARATION OF INTERESTS

L. Ren, C. Liu, P. Ding, Z. Qian and L.Q. Ren are patent holders on the development of HimiSK actuator with variable gearing mechanism.

Received: June 16, 2021
Revised: August 5, 2021
Accepted: August 19, 2021
Published: September 24, 2021

REFERENCES

Alici, G. (2018). Softer is harder: what differentiates soft robotics from hard robotics? MRS Adv. *3*, 1557–1568. https://doi.org/10.1557/adv.2018.159.

Azizi, E., Brainerd, E.L., and Roberts, T.J. (2008). Variable gearing in pennate muscles. Proc. Natl. Acad. Sci. U S A *105*, 1745–1750. https://doi.org/10.1073/pnas.0709212105.

Bahler, A.S. (1968). Modeling of mammalian skeletal muscle. IEEE Trans. Biomed. Eng. *15*, 249–257. https://doi.org/10.1109/tbme.1968.4502575.

Ball, E.J., Meller, M.A., Chipka, J.B., and Garcia, E. (2016). Modeling and testing of a knitted-sleeve fluidic artificial muscle. Smart Mate. Struct. *25*, 115024. https://doi.org/10.1088/0964-1726/25/11/115024.

Biewener, A.A. (2016). Locomotion as an emergent property of muscle contractile dynamics. J. Exp. Biol. *219*, 285–294. https://doi.org/10.1242/jeb.123935.

Brainerd, E.L., and Azizi, E. (2005). Muscle fiber angle, segment bulging and architectural gear ratio in segmented musculature. J. Exp. Biol. *208*, 3249–3261. https://doi.org/10.1242/jeb.01770.

Brown, I.E., and Loeb, G.E. (2000). A reductionist approach to creating and using neuromusculoskeletal models. In Biomechanics and Neural Control of Posture and Movement, J.M. Winters and P.E. Crago, eds., pp. 148–163. https://doi.org/10.1007/978-1-4612-2104-3_10.

Chou, C.P., and Hannaford, B. (1996). Measurement and modeling of McKibben pneumatic artificial muscles. IEEE Trans. Robot. Autom. *12*, 90–102. https://doi.org/10.1109/70.481753.

Chun, K.Y., Kim, S.H., Shin, M.K., Kwon, C.H., Park, J., Kim, Y.T., Spinks, G.M., Lima, M.D., Haines, C.S., Baughman, R.H., and Kim, S.J. (2014). Hybrid carbon nanotube yarn artificial muscle inspired by spider dragline silk. Nat. Commun. *5*, 3322. https://doi.org/10.1038/Ncomms4322.

Cianchetti, M., Laschi, C., Menciassi, A., and Dario, P. (2018). Biomedical applications of soft robotics. Nat. Rev. Mater. *3*, 143–153. https://doi.org/10.1038/s41578-018-0022-y.

Daley, M.A., Voloshina, A., and Biewener, A.A. (2009). The role of intrinsic muscle mechanics in the neuromuscular control of stable running in the Guinea fowl. J. Physiol. *587*, 2693–2707. https://doi.org/10.1113/jphysiol.2009.171017.

Duduta, M., Wood, R.J., and Clarke, D.R. (2016). Multilayer dielectric elastomers for fast, programmable actuation without prestretch. Adv. Mater. *28*, 8058–8063. https://doi.org/10.1002/adma.201601842.

Gaylord, R.H. (1958). Fluid Actuated Motor System and Stroking Device, US Patent No.2844126.

Geyer, H., Seyfarth, A., and Blickhan, R. (2003). Positive force feedback in bouncing gaits? Proc. Biol. Sci. *270*, 2173–2183. https://doi.org/10.1098/rspb.2003.2454.

Haeufle, D.F.B., Grimmer, S., and Seyfarth, A. (2010). The role of intrinsic muscle properties for stable hopping-stability is achieved by the force-velocity relation. Bioinspir. Biomim. *5*, 16004. https://doi.org/10.1088/1748-3182/5/1/016004.

Haeufle, D.F.B., Gunther, M., Blickhan, R., and Schmitt, S. (2012). Proof of concept: model based bionic muscle with hyperbolic force-velocity relation. Appl. Bionics. Biomech. *9*, 267–274. https://doi.org/10.1155/2012/146909.

Hill, A.V. (1938). The heat of shortening and the dynamic constants of muscle. Proc. R. Soc. B Biol. Sci. *126*, 136–195. https://doi.org/10.1098/rspb.1938.0050.

Ijspeert, A.J. (2014). Biorobotics: using robots to emulate and investigate agile locomotion. Science *346*, 196–203. https://doi.org/10.1126/science.1254486.

Josephson, R.K. (1993). Contraction dynamics and power output of skeletal muscle. Annu. Rev. Physiol. *55*, 527–546. https://doi.org/10.1146/annurev.ph.55.030193.002523.

Klute, G.K., and Czerniecki, J.M. (1999). McKibben Artificial Muscles: Pneumatic Actuators with Biomechanical Intelligence. In IEEE International Conference on Advanced Intelligent Mechatronics, Atlanta, USA, 221-226. https://doi.org/10.1109/AIM.1999.803170.

Klute, G.K., Czerniecki, J.M., and Hannaford, B. (2002). Artificial muscles: actuators for biorobotic systems. Int. J. Robot. Res. *21*, 295–309. https://doi.org/10.1177/027836402320556331.

Kurumaya, S., Suzumori, K., Nabae, H., and Wakimoto, S. (2016). Musculoskeletal lower-limb robot driven by multifilament muscles. ROBOMECH J. *3*. https://doi.org/10.1186/s40648-016-0061-3.

Lima, M.D., Li, N., de Andrade, M.J., Fang, S.L., Oh, J., Spinks, G.M., Kozlov, M.E., Haines, C.S., Suh, D., Foroughi, J., et al. (2012). Electrically, chemically, and photonically powered torsional and tensile actuation of hybrid carbon nanotube yarn muscles. Science *338*, 928–932. https://doi.org/10.1126/science.1226762.

Loeb, G.E., Brown, I.E., and Cheng, E.J. (1999). A hierarchical foundation for models of sensorimotor control. Exp. Brain Res. *126*, 1–18. https://doi.org/10.1007/s002210050712.

Marsh, R.L. (1999). How muscles deal with real-world loads: the influence of length trajectory on muscle performance. J. Exp. Biol. *202*, 3377–3385. https://doi.org/10.1242/jeb.202.23.3377.

McCracken, J.M., Donovan, B.R., and White, T.J. (2020). Materials as machines. Adv. Mater. *32*, 1906564. https://doi.org/10.1002/adma.201906564.

Mccrorey, H.L., Gale, H.H., and Alpert, N.R. (1966). Mechanical properties of cat tenuissimus muscle. Am. J. Physiol. *210*, 114–120. https://doi.org/10.1152/ajplegacy.1966.210.1.114.

Mintchev, S., and Floreano, D. (2016). Adaptive morphology A design principle for multimodal and multifunctional robots. IEEE Robot. Autom. Mag. *23*, 42–54. https://doi.org/10.1109/Mra.2016.2580593.

Mirvakili, S.M., and Hunter, I.W. (2018). Artificial muscles: mechanisms, applications, and challenges. Adv. Mater. *30*, 1704407. https://doi.org/10.1002/adma.201704407.

Mu, J.K., de Andrade, M.J., Fang, S.L., Wang, X.M., Gao, E.L., Li, N., Kim, S.H., Wang, H.Z., Hou, C.Y., Zhang, Q.H., et al. (2019). Sheath-run artificial muscles. Science *365*, 150–155. https://doi.org/10.1126/science.aaw2403.

Neptune, R.R., McGowan, C.P., and Fiandt, J.M. (2009). The influence of muscle physiology and advanced Technology on sports performance. Annu. Rev. Biomed. Eng. *11*, 81–107. https://doi.org/10.1146/annurev-bioeng-061008-124941.

Nickel, V.L., Perry, J., and Garrett, A.L. (1963). Development of useful function in the severely paralyzed hand. J. BoneJoint Surg. *45*, 933–952. https://doi.org/10.2106/00004623-196345050-00004.

Pfeifer, R., Lungarella, M., and Iida, F. (2007). Self-organization, embodiment, and biologically inspired robotics. Science *318*, 1088–1093. https://doi.org/10.1126/science.1145803.

Rack, P.M., Ross, H.F., Thilmann, A.F., and Walters, D.K. (1983). Reflex responses at the human ankle: the importance of tendon compliance. J. Physiol. *344*, 503–524. https://doi.org/10.1113/jphysiol.1983.sp014954.

Ralston, H.J., Polissar, M.J., Inman, V.T., Close, J.R., and Feinstein, B. (1949). Dynamic features of human isolated voluntary muscle in isometric and free contractions. J. Appl. Physiol. *1*, 526–533. https://doi.org/10.1152/jappl.1949.1.7.526.

Roche, E.T., Wohlfarth, R., Overvelde, J.T.B., Vasilyev, N.V., Pigula, F.A., Mooney, D.J., Bertoldi, K., and Walsh, C.J. (2014). A bioinspired soft actuated material. Adv. Mater. *26*, 1200–1206. https://doi.org/10.1002/adma.201304018.

Saga, N., Nakamura, T., Uehara, J., and Iwade, T. (2003). Development of Artificial Muscle Actuator Reinforced by Kevlar Fiber. In IEEE International Conference on Industrial Technology, Bangkok, Thailand, 950-954. https://doi.org/10.1109/ICIT.2002.1189297.

Saga, N., and Saikawa, T. (2012). Development of a pneumatic artificial muscle based on biomechanical characteristics. Adv. Robot. *22*, 761–770. https://doi.org/10.1163/156855308x305317.

Schmitt, S., Haeufle, D.F.B., Blickhan, R., and Gunther, M. (2012). Nature as an engineer: one simple concept of a bio-inspired functional artificial muscle. Bioinspir. Biomim. *7*, 036022. https://doi.org/10.1088/1748-3182/7/3/036022.

van Soest, A.J., and Bobbert, M.F. (1993). The contribution of muscle properties in the control of explosive movements. Biol. Cybern. *69*, 195–204. https://doi.org/10.1007/BF00198959.

Wagner, H., and Blickhan, R. (1999). Stabilizing function of skeletal muscles: an analytical investigation. J. Theor. Biol. *199*, 163–179. https://doi.org/10.1006/jtbi.1999.0949.

Wilkie, D.R. (1956). The mechanical properties of muscle. Br. Med. Bull. *12*, 177–182. https://doi.org/10.1093/oxfordjournals.bmb.a069546.

Yang, G.Z., Bellingham, J., Dupont, P.E., Fischer, P., Floridi, L., Full, R., Jacobstein, N., Kumar, V., McNutt, M., Merrifield, R., et al. (2018). The grand challenges of Science Robotics. Sci. Robot. *3*, eaar7650. https://doi.org/10.1126/scirobotics.aar7650.

Yamamoto, Y., Wakimoto, S., Suzumori, K., and Wada, A. (2012). J113033 development of miniature McKibben actuator. Proc. Mech. Eng. Congress Jpn. *2012*, J1130333-1–J113033-3. https://doi.org/10.1299/jsmemecj.2012._J113033-1.

STAR★METHODS

KEY RESOURCES TABLE

REAGENT or RESOURCE	SOURCE	IDENTIFIER
Software and algorithms		
Matlab R2016a	MathWorks	https://www.mathworks.com
Origin 9.1 (2019)	Originlab	https://www.originlab.com
Premiere Pro 6.0	Adobe	https://www.adobe.com
Unigraphics NX10.0	Siemens PLM Software	http://www.siemens.com/plm
Abaqus 2019	Dassault SIMULIA	www.simulia.com
Other		
DYB-5 dynamic strain measuring instrument	Beidaihe Practical Electronics Technology Institute	http://www.bdhsd.com
Aixplorer ultrasound scanner	SuperSonic Imagine Ltd.	www.supersonicimagine.com
VIBSYS vibration signal acquisition and analysis instrument	Beijing Wavespectrum Science and Technology Co.,Ltd.	www.earthquake.com.cn
Phantom v711	Vision Research	https://www.visionresearch.com.es

RESOURCE AVAILABILITY

Lead contact

Further information and requests for resources and reagents should be directed and will be fulfilled by the Lead Contact, Lei Ren (lei.ren@manchester.ac.uk).

Materials availability

This study did not generate new unique reagents.

Data and code availability

Original/source data in this study is available upon request. All original code is available in this paper's supplemental information. Any additional information required to reanalyze the data reported in this study is available from the lead contact upon request.

METHODS DETAILS

Fabrication of actuators

PA30-Matrix or PA0-Matrix actuator consists of five MFUs embedded in a flexible matrix. For each MFU, an elastic circular tube (outer diameter: 10 mm, inner diameter: 6 mm) was fabricated by pouring prepared Dragon Skin 20 mixture into a 3D printed mould with both ends sealed in a beaker. Each elastic tube was sheathed in a Nylon mesh with one end fastened by a nylon cable tie and the other end sintered by heating, forming the final MFU (length: 110 mm, diameter: 10 mm). A parallelogram shaped mould with the acute side angle being 30° was used to cast the flexible matrix for the PA30-Matrix actuator, whereas a rectangle mould was used for the PA0-Matrix actuator. The five MFUs were placed in parallel in the mold with evenly distributed spacing, and Dragon Skin 20 mixture was then poured into the mold. The flexible matrix was finally solidified at room temperature for 6 hours. The PA30-NoMatrix actuator consists of five MFUs and two end plates. Firstly, the five MFUs were arranged in parallel in a parallelogram mould same as that used in making the PA30-Matrix actuator. Two plate shaped cavities with 10 mm thickness were formed by using Teflon tape at both edges of the mould. Then Polyurethane resin Smooth-cast 300 (Smooth-On Inc., USA) was poured into each cavity until all the ends of MFUs were fully immersed, and the two end plates were cured for 1 minute. Finally, the PA30-NoMatrix actuator was fabricated.

The semimembranosus HimiSK actuator consists of ten MFUs (outer diameter: 6 mm, inner diameter: 4 mm) embedded in a flexible matrix. A three-part mould was 3D printed including left and right shaping parts and one core part. Ten MFUs with tube connectors were inserted in the core mould which was placed in

the right shaping mould. Dragon skin 20 mixture was poured into the left shaping mould, and then the three-part mould was assembled by putting the right and left parts together. After cured in room temperature for 6 hours, the right shaping mould and the core mould were removed. Dragon skin 20 mixture was then poured into the right shaping mould without the core mould. Once the right shaping mould had been completely filled, the two shaping moulds were slowly closed and cured at room condition for 6 hours. The finished semimembranosus HimiSK actuator has a length of 225.28 mm and a maximum thickness of 60 mm.

Force-velocity test and data collection

A customised experimental test-rig was constructed to characterise the force-velocity properties of the HimiSK actuators (Figure S1). An air compressor (BKB-0.11/8, Quanzhou Jiebao Ltd., China) provided air supply for the actuators. The actuation air pressure was controlled by a pressure regulator (IR2000-02BG, SMC, Japan), together with a compensated flow control valve (GR-3/8-B 6308, FESTO, Germany). The PA30-Matrix, PA30-NoMatrix and PA0-Matrix actuators were tested at 0.04, 0.08, 0.12, 0.16, 0.20 MPa, and the actuators acted against 6 different loads ranging from 0 to 100% of the maximum load F0 with a 20% F0 increment. The test was repeated six times at each load for each pressure. A S-type force sensor (CGQ-YS, Bengbu Tongli Ltd., China) was used to measure the actuator force. A laser displacement sensor (HG-C1100, Panasonic, Japan) was employed to record the actuator displacement. The force sensor data was first collected by using a DYB-5 dynamic strain measuring instrument (Beidaihe Practical Electronics Technology Institute, Hebei, China), and then a VIBSYS vibration signal acquisition and analysis instrument (Beijing Wavespectrum Science and Technology Co.,Ltd, China) was used for the data acquisition.

The collected force and displacement data were processed and analysed using MATLAB software (MathWorks Inc., USA), and the actuator velocity was calculated by differentiating the displacement data over time. The averaged actuator shortening velocities and averaged actuator forces in the peak shortening velocity zone during isotonic contractions were used to quantify the actuator force-velocity properties (Figure S2). A peak shortening velocity zone (the grey zones in Figure S2) with a duration of 0.1s was defined, where the maximum shortening velocity is achieved in the middle of the zone whilst the actuator force reaches a steady state. Thereafter, the average shortening velocity and average actuator force within this zone were used to quantify the actuator force-velocity property. At each actuation pressure and each load, the velocity was collected for six times, then calculate its average and variance. The relation of force and velocity was obtained.

Thickness, pennation angle and AGR test

To quantify the MFU contraction velocity and the changes in actuator pennation angle and thickness, we used a digital camera (EOS 850D, Canon, Japan) to record the actuator behaviour at 30 frames per second. The recorded video was converted to still images using Premiere Pro 6.0 software (Adobe, USA). The images of two key frames at the beginning and at the end of the peak shortening velocity zone during isotonic contractions were analysed in Unigraphics NX software (Siemens PLM, USA). The raster image tool was used to acquire the length of the middle MFU in the array by measuring from the mid-point of the Nylon cable to the mid-point of the terminal sintered end. The MFU shortening velocity was calculated as the MFU length change between the two frames divided by the duration of the peak shortening velocity zone. To determine the changes in actuator pennation angle and thickness, we selected two key frames corresponding to the instant just before the load was off the surface and also the instant when the maximum shortening velocity was reached respectively. The two images were analysed in Unigraphics NX software (Siemens PLM, USA) using the raster image tool. The acute angle between the middle MFU and the left side of the actuator was measured as the pennate angle. The thickness was determined by measuring the distance between the leftmost and the rightmost points of the actuator. The differences between the measured values at the two frames were the changes in the actuator pennation angle and thickness. The measuring for each individual value was repeated three times. Finally, the AGR was calculated as the ratio of the actuator shortening velocity over the contraction velocity of the middle MFU.

The load-dependent changes in pennation angles and thicknesses of the PA30-Matrix, PA0-Matrix and PA30-NoMatrix actuators at five different activation pressures (0.04, 0.08, 0.012, 0.16, 0.20 MPa) are shown in Figure S3. We can see consistently increased pennation angle and actuator thickness with increased activation pressure for all three actuators. Similar to skeletal muscle, increasing applied load generally results in decreased pennation angle and actuator thickness.

FEM simulation of PA30-Matrix actuator

The finite element model of the PA30-Matrix actuator was constructed using Abaqus 2019 (Simulia, USA), which consists of five MFUs embedded in a flexible matrix. The MFUs and the soft matrix were assumed to be homogeneous and isotropic with linear elastic material properties. The MFU was simplified as closed circular tube with linear elastic material (Young's modulus 1.5 MPa, Poisson's ratio 0.31) (Roche et al., 2014). Double symmetrical rebar layers (Young's modulus 100MPa, Poisson's ratio 0.3) were used to simulate the nylon meshes wrapping around the elastic tube. The entire flexible matrix was defined as linear elastic material with Young's modulus of 0.6 MPa and Poisson's ratio of 0.475 (Alici, 2018). The interaction between the MFUs and the flexible matrix was defined as tie constraint, and fluid cavity (pneumatic type) interaction property was used to simulate the inflation behaviour of the MFUs upon pressurised. The MFUs and the flexible matrix were meshed using a total number of 1183 and 14099 quadratic tetrahedral (C3D10) elements respectively, which were determined through a convergence analysis by gradually increasing the mesh density until the deviations in the estimated stresses reached within 5%.

In order prove that synergy of MFUs in a flexible matrix, we have carried on five simulations based on the model of PA30-matrix. The PA30-matrix actuators were actuated by only one MFU, then two, three, four and five MFUs respectively, under the zero loads at 0.2MPa. The predicted displacement (Figure S4) increases with increased number of MFUs. The parameters scale is approach to linearly. And, the predicted distributions of the intermediate and minimum principal stresses and strains of PA30-Matrix actuator were shown in Figure S5.

Analysis of work density and efficiency

Based on the PA30-Matrix actuator numerical simulation, we can also obtain the relative pressure (P) and the volume change of MFUs (V_i). Therefore, the work density (the work per actuator volume the actuators provide during one cycle actuation) and efficiency (η) of PA30-Matrix actuator at 0.2MPa was calculated. The work density ($W_{density}$) and efficiency (η) were calculated by the following formulation.

$$w_{density} = \frac{W_{in}}{v_a} = \frac{\sum_{i=1}^{5} \int_0^{V_{max}} P dv_i}{v_a} = 15.35 \mathrm{kJ/m^3}$$

$$\eta = \frac{w_{out}}{w_{in}} = \frac{F \cdot S}{\sum_{i=1}^{5} \int_0^{V_{max}} P dv_i} = 4.38\%$$

W_{in} is the input work. V_a represents the volume of actuator. i represents the number of MFUs. P and dV_i are obtained from simulation. The total input work is 0.00274 kJ. W_{out} is the maximum output work, F is the output force, S is the displacement of soft actuator. The change of output work with different loads of PA30-Matrix actuator is shown in Figure S6. The maximum output work is corresponding to a load of 16 N, and the W_{out} is about 0.12 N·m. There is a gap compared with those of skeletal muscle due to the reduced strain of MFU casing by the addition of flexible matrix. Nevertheless, these limitations will be addressed in future work by changing the materials of actuator, or changing its connected methods with loads.

Ultrasound muscle measurement

To inform the design and fabrication of the semimembranosus HimiSK actuator, the pennation angle of the left semimembranosus muscle of a healthy male subject was measured using a linear transducer (10-2 MHz) provided by an Aixplorer ultrasound scanner (SuperSonic Imagine Ltd., France) at B-mode. The subject was examined while lying prone with the left knee fully extended, and then the probe was located in the middle of the left semimembranosus muscle. After the probe was firmly placed, the subject was instructed to lift the calf slowly to flex the knee joint. Five second video was recorded, and then converted to still images using Premiere Pro 6.0 software (Adobe, USA). Two images were selected with one at the rest position and the other at the most flexed knee position. The raster image tool in the Unigraphics NX software (Siemens PLM Ltd., USA) was used to measure the muscle pennation angle, which was defined as the acute angle between the muscle fibre and the fascia.

Force-length property test

To measure the force-length characteristic of the semimembranosus HimiSK actuator, a customised experimental test-rig was constructed to perform isometric contractions (Figure S7). The actuator was placed horizontally with both ends fixed during contractions. The actuator length is adjusted by repositioning the two movable ends. An air compressor was used to activate the actuator, which was tested at ten different lengths under five pressures (0.08, 0.12, 0.16, 0.20, 0.24 MPa). Each test was repeated three times. The actuator force was measured by two force sensors fixed at both ends.

Geometric details for robotic arm

A robotic arm was constructed to conduct the impact perturbation tests (Figure S8), which consists of an upper arm and a forearm made of aluminum (6061) with a total weight of 0.9 kg. The upper arm and forearm were connected by an elbow joint with an axle and two bearings (619/5ZZ/P5, BPJ, Japan). Two identical actuators were placed vertically and symmetrically with respect to the upper arm. An air cylinder (MAL25×100 CA, Airtac Ltd., China) was positioned vertically above or below the forearm end to apply downwards or upwards impact perturbation. The air cylinder was regulated by a valve IR2000-02BG (SMC Ltd., Japan) controlled by a control board (Apollo STM32429IGTx, Eixpsy Ltd., China) to provide consistent and repeatable impact forces.

Impact perturbation experiments

A robotic arm consisting of a fixed upper arm and a moving forearm was constructed. The elbow joint was regulated by an antagonistic pair of identical semimembranosus HimiSK actuators or identical McKibben pneumatic actuators. The two McKibben muscles were fabricated using the same method and materials for making the MFUs, which have a very similar dimension (length 200mm, outer diameter 26 mm, inner diameter 4.5 mm) to the semimembranosus HimiSK actuator and also produce same amount of force as the HimiSK actuator upon pressurised. An air cylinder MAL 25×100CA (Airtac Ltd., China) powered by an air pump OTS 4×750W-120L (Outstanding Ltd., China) was used to apply downwards or upwards impact perturbation to the end of the forearm. To provide consistent impact force, the cylinder was pumped at a pressure of 0.5 MPa for 25 ms regulated by a valve IR2000-02BG (SMC Ltd., Japan) manipulated by a control board (Apollo STM32429IGTx, Eixpsy Ltd., China). The downwards and upwards impact perturbation experiments were conducted on the robotic arm with the HimiSK actuators or McKibben actuators activated at 0.05 MPa and 0.20 MPa respectively. The test was repeated four times for each condition.

To quantify the robotic arm motion, a maker with a diameter of 3 mm was placed at the end of the forearm. A high-speed camera (Phantom v711, Vision Research, USA) was used to record the dynamic behaviour of the robotic arm at 1000 Hz. We imported the videos to Matlab software (MathWorks Inc., USA), and using its VideoReader function. The marker coordinates (X, Y) were then determined for each frame by defining the centroid of the elbow joint as the origin and the line connecting the origin and the marker centroid as the X axis in the stationary state without perturbations. Finally, the forearm angle was calculated as the angle between the forearm axis (connecting the elbow joint centroid and the marker centroid) and the X axis.